

## Full paper

# Interfacial engineering in colloidal “giant” quantum dots for high-performance photovoltaics

Gurpreet S. Selopal<sup>a,b</sup>, Haiguang Zhao<sup>c,\*</sup>, Guiju Liu<sup>c</sup>, Hui Zhang<sup>b</sup>, Xin Tong<sup>a,b</sup>, Kanghong Wang<sup>b,d</sup>, Jie Tang<sup>c</sup>, Xuhui Sun<sup>d</sup>, Shuhui Sun<sup>b</sup>, François Vidal<sup>b</sup>, Yiqian Wang<sup>c</sup>, Zhiming M. Wang<sup>a,\*</sup>, Federico Rosei<sup>a,b,\*\*</sup>

<sup>a</sup> Institute of Fundamental and Frontier Sciences, University of Electronic Science and Technology of China, Chengdu 610054, PR China

<sup>b</sup> Institut National de la Recherche Scientifique, Centre Énergie, Matériaux et Télécommunications, 1650 Boul. Lionel Boulet, Varennes, Québec, Canada J3X 1S2

<sup>c</sup> College of Physics & State Key Laboratory, Qingdao University, No. 308 Ningxia Road, Qingdao 266071, PR China

<sup>d</sup> Institute of Functional Nano & Soft Materials, Soochow University, Suzhou, Jiangsu 215123, PR China

## ARTICLE INFO

## Keywords:

Quantum dot  
Giant-core/shell  
Alloyed interfacial layer  
Interface engineering  
Carrier transport  
Solar cells

## ABSTRACT

Colloidal quantum dots (QDs) are semiconductor nanocrystals which exhibit discrete energy levels. They are promising building blocks for optoelectronic devices, thanks to their tunable band structure. Here, we explore a nanoengineering approach to highlight the influence of an alloyed interface on the optical and electronic properties of CdSe/(CdS)<sub>6</sub> “giant” core/shell (CS) QDs by introducing CdSe<sub>x</sub>S<sub>1-x</sub> interfacial layers between core and shell. By incorporating of CdSe<sub>x</sub>S<sub>1-x</sub> interfacial layers, CdSe/(CdSe<sub>x</sub>S<sub>1-x</sub>)<sub>4</sub>/(CdS)<sub>2</sub> (x = 0.5) core/shell (CSA1) QDs exhibit a broader absorption response towards longer wavelength and higher electron-hole transfer rate due to favorable electronic band alignment with respect to CS QDs, as confirmed by optical absorption, photoluminescence (PL) and transient fluorescence spectroscopic measurements. In addition, simulations of spatial probability distributions show that the interface layer enhances electron-hole spatial overlap. As a result, CSA1 QDs sensitized solar cells (QDSCs) yield a maximum photoconversion efficiency (PCE) of 5.52%, which is 79% higher than QDSCs based on reference CS QDs. To fully demonstrate the structural interface engineering approach, the CdSe<sub>x</sub>S<sub>1-x</sub> interfacial layers were further engineered by tailoring the selenium (Se) and sulfur (S) molar ratios during in situ growth of each interfacial layer. This graded alloyed CdSe/(CdSe<sub>x</sub>S<sub>1-x</sub>)<sub>5</sub>/(CdS)<sub>1</sub> (x = 0.9–0.1) core/shell (CSA2) QDs show a further broadening of the absorption spectrum, higher carrier transport rate and modified confinement potential with respect to CSA1 QDs as well as reference CS QDs, yielding a PCE of 7.14%. Our findings define a promising approach to improve the performance of QDSCs and other optoelectronic devices based on CS QDs.

## 1. Introduction

Colloidal quantum dots (QDs) have been widely studied for potential applications in multiple emerging technologies, including photovoltaic devices such as QDs sensitized solar cells (QDSCs) [1], single [2] or multi-junction [3] colloidal QDs solar cells and photodetectors [4], bio-sensors [5], light emitting diodes (LED) [6], luminescent solar concentrators (LSCs) [7] etc., due to their versatile optoelectronic properties, such as size/composition-tunable absorption band edge [8], high absorption coefficient [9] and large intrinsic dipole moments [10]. In particular, as light absorbing materials in QDSCs, the possibility of multiple exciton generation (MEG) [11] and hot electron extraction

[12] could boost the theoretical photoconversion efficiency (PCE) of the QDSCs beyond the Shockley–Queisser limit of 32.7% [13,14]. Recently, a record certified PCE of 12.07% [15] was reported for QDSCs using ZnCuInSe QDs sensitized photoanodes and nitrogen-doped mesoporous carbon (N-MC) as counter electrodes (CEs) and 13.4% was reported for CsPbI<sub>3</sub> QDs [16]. These record values of PCEs are still substantially lower than that of commercial single-crystal silicon solar cells (~20%) [17] and emerging organo-inorganic hybrid perovskite solar cells (over 20%) [18]. The possible reasons of this relatively low PCE of QDSCs are mainly associated with narrow light harvesting range of QDs [19], slow charge injection/transfer rate from QDs to electron/hole acceptors [20] and fast undesirable non-radiative carrier recombination due to the

\* Corresponding authors.

\*\* Corresponding author at: Institute of Fundamental and Frontier Sciences, University of Electronic Science and Technology of China, Chengdu 610054, PR China.  
E-mail addresses: [hgzhao@qdu.edu.cn](mailto:hgzhao@qdu.edu.cn) (H. Zhao), [zhmwang@uestc.edu.cn](mailto:zhmwang@uestc.edu.cn) (Z.M. Wang), [rosei@emt.inrs.ca](mailto:rosei@emt.inrs.ca) (F. Rosei).

<https://doi.org/10.1016/j.nanoen.2018.11.001>

Received 6 August 2018; Received in revised form 26 October 2018; Accepted 1 November 2018

Available online 02 November 2018

2211-2855/ © 2018 Elsevier Ltd. All rights reserved.

presence of surface traps/defects at interfaces as well as within the QDs during device operation [21]. Employing the core/shell architecture in which a QD core is coated with shell layers of different materials/thickness is an effective approach to address these challenges [22,23]. Core/shell QD architecture offers a reduced density of surface trap states/defects and an enhanced spatial separation of electron and hole (forming a quasi-type-II band structure in which the electrons leak into the shell region, while the holes are confined within the core QD) that significantly improves the quantum yield (QY), prolonged photoluminescence (PL) lifetime and endows the QDs with better chemical, thermal and photo-chemical/physical stability compared to bare QDs [24–26].

Among various kinds of core/shell QDs, a specially designed QDs called “giant” core/shell QDs composed of a core QD covered with the relatively thick shell (several nanometers up to tens of nanometers), have been widely studied for applications in optoelectronic devices [27,28] and energy conversion devices [29–31]. In the “giant” core/shell QDs, the formation of surface traps and surface oxidation of the core QD is largely reduced due to the efficient isolation of core QD from the surrounding chemical environments by thick shell materials. This thick shell of “giant” QDs can significantly improve the optoelectronic properties, such as superior photo-physical/chemical stability, suppressed non-radiative Auger recombination, improved QY and prolonged multi-exciton lifetime compared to both pure QDs and core/thin-shell (shell thickness  $\leq 1.5$  nm) QDs [32–35]. Most importantly, this “giant” QDs heterostructure allows the formation of a quasi-type II band alignment [33,36,37]. Usually, in “giant” QDs, for example, CdSe/(CdS)<sub>6</sub> QDs (denoted as CS QDs), the interfacial strain at the sharp interface of CdSe core and CdS shell caused by the lattice mismatch (4.4%) between CdSe and CdS [38] leads to the formation of interfacial defects and undesirable carrier confinement potential [33,39]. In addition, due to the thick shell of CdS over the CdSe core QD, the absorption spectrum of CS QDs is dominated by the CdS shell ( $E_g = 2.49$  eV), which absorb strongly in the ultraviolet (UV) and partially in the visible range (below 500 nm) [40]. In addition, the thick CdS shell acts as a physical and energy barrier potential for electron/hole injection processes [41]. Therefore, this requires the optimization of the electron/hole injection rate and efficient surface passivation of CS QDs by interfacial engineering of the core/shell architecture. Recently, Bae et al. demonstrated that the presence of the interfacial layer between the CdSe/CdS core/shell sharp interface leading to significant suppression of Auger recombination [42]. We also observed that the presence of the interfacial layer between the core and shell of “giant” core/shell QDs generates double color emission [43]. These findings allow us to optimize the architecture of CS QDs towards improving the electron/hole injection rate, while maintaining efficient surface passivation.

Herein, we report the design and synthesis of “giant” core/shell QDs with an engineered interfacial layer between the core and shell to improve optoelectronic properties of CS QDs. First, we synthesized CdSe core QDs ( $R = 1.65$  nm), followed by CdS shell with engineered CdSe<sub>x</sub>S<sub>1-x</sub> interfacial layers deposition via a successive ionic layer adsorption and reaction (SILAR) approach (see Experimental Section). The crystal structure of as-synthesized QDs was investigated by using high-resolution transmission electron microscopy (HR-TEM) and X-ray diffraction (XRD). Optical properties of QDs with engineered interfacial layer demonstrated the broadening of absorption and PL spectra towards longer wavelength. The presence of the CdSe<sub>x</sub>S<sub>1-x</sub> interfacial layers at the sharp core/shell QDs interface significantly enhances the electron injection rate, as confirmed by transient PL lifetime investigation. This newly engineered CdSe/(CdSe<sub>0.5</sub>S<sub>0.5</sub>)<sub>4</sub>/(CdS)<sub>2</sub> “giant” core/alloved shell QDs (denoted as CSA1 QDs) based QDSC obtained a PCE of 5.52% under one sun simulated sunlight at AM 1.5 G (100 mW/cm<sup>2</sup>), which is approximately 79% higher than the reference CS QDs based QDSCs. To further improve the optoelectronic properties of CSA1 QDs, and specifically to increase the PCE of the device, we engineered the CdSe<sub>x</sub>S<sub>1-x</sub> interfacial layers by tailoring the selenium (Se) and sulfur

(S) ratio in each layer between CdSe core and CdS shell. The QDSC based on CdSe/(CdSe<sub>x</sub>S<sub>1-x</sub>)<sub>5</sub>/(CdS)<sub>1</sub> ( $x = 0.9–0.1$ ) “giant” core/shell QDs (denoted as CSA2 QDs) exhibited a PCE of 7.14%, thanks to CdSe<sub>x</sub>S<sub>1-x</sub> ( $x = 0.9–0.1$ ) graded alloyed interfacial layers at the sharp interface of CdSe core and CdS shell of CS QDs. This opens a route to improve the optoelectronic properties of CS QDs for efficient energy conversion as well as for other optoelectronic technologies.

## 2. Experimental section

### 2.1. Materials

Sulfur (100%), oleylamine (OLA) (technical grade, 70%), cadmium oxide (99%), cadmium nitrate tetra hydrate ( $\geq 99\%$ ), oleic acid (OA), Rhodamine 6G and octadecene (ODE), selenium pellet ( $\geq 99.999\%$ ), trioctyl phosphine oxide (TOPO), trioctyl phosphine (TOP) (97%), hexane, zinc acetate dihydrate (98%), sodium hydroxide, sodium sulfide nonahydrate ( $\geq 99.9\%$ ), titanium tetrachloride (30%), hydrochloric acid, toluene, methanol, acetone, ethanol and isopropanol (IPA) were obtained from Sigma-Aldrich Inc.

TiO<sub>2</sub> pastes composed of 20 nm sized anatase nanoparticles (Transparent, Code 18 NR-T) and larger 150–250 nm sized anatase scattering particles (Opaque, code WER2-O) were supplied by Dyesol. Transparent Fluorine doped tin oxide (FTO) coated conducting glass substrates with sheet resistance 10  $\Omega$ /square were bought from Pilkington glasses. All chemicals were used as purchased without any purification.

### 2.2. QD synthesis

CdSe QDs of diameter (3.3 nm) were synthesized by using a hot injection approach [44]. In brief, TOPO (1 g) and Cd-oleate (0.38 mmol, 1 mL) in 8 mL of ODE were purged by N<sub>2</sub> at room temperature for 30 min. The reaction system was evacuated for 30 min at 100 °C, and then the temperature was raised to 300 °C. The mixture of TOP-Se (4 mmol, 4 mL), 3 mL of OLA, and 1 mL of ODE at room temperature was quickly injected into the Cd-oleate suspension under vigorous stirring. The reaction cell was quenched with cold water after injection. Ethanol (20 mL) was added, then the suspension was centrifuged. The supernatant was removed and finally, the QDs were dispersed in toluene and kept at  $-10$  °C in the refrigerator. Deposition of CdS layers on CdSe QDs was performed by SILAR, similar to the procedure described in Ghosh et al. [45] Typically, in a 100 mL round-bottom flask, OLA (5 mL), ODE (5 mL) and CdSe QDs ( $\sim 2 \times 10^{-7}$  mol in hexane) were degassed at 110 °C for 30 min. The reaction flask was re-stored with N<sub>2</sub> and the temperature was further raised to 240 °C with stirring. The Cd(OA)<sub>2</sub> dispersed in ODE (0.25 mL, 0.2 M) was added dropwise and the mixture allowed to react for 2.5 h, followed by dropwise addition of 0.2 M sulfur in ODE with the same volume. The shell was further annealed for 10 min. All subsequent shells were annealed at 240 °C for  $\sim 10$  min following the injection of sulfur and  $\sim 2.5$  h following dropwise addition of the Cd(OA)<sub>2</sub> in ODE. Sulfur/Cd(OA)<sub>2</sub> addition volumes for shell addition cycles one-six were as follows: 0.25, 0.36, 0.49, 0.63, 0.8, and 0.98 mL, respectively. The reaction was cooled to room temperature using cold water. Ethanol was added, then the suspension was centrifuged and the supernatant was removed. The QDs were then dispersed in toluene for further characterization and labeled hereafter as “CS” for CdSe core with six cycles of CdS shells QDs (details of the core/shell size/shell thickness are reported in Table 1).

We used a mixture of 0.2 M Se and S in ODE as precursors (following the same procedure as mentioned above for four cycles of CdSe<sub>0.5</sub>S<sub>0.5</sub>) for the synthesis CdSe/CdS core/shell QDs with an interfacial alloyed CdSe<sub>x</sub>S<sub>1-x</sub> layer, with  $x = 0.5$ . Finally, two monolayers of CdS were added to interfacial alloyed CdSe<sub>0.5</sub>S<sub>0.5</sub> to synthesize CSA1 QDs. Similarly, one-five monolayers of interfacial alloyed CdSe<sub>x</sub>S<sub>1-x</sub> over the

**Table 1**  
Optoelectronic parameters of the as-synthesized QDs in toluene and QDs deposited on TiO<sub>2</sub> mesoporous film.

QDs structure	R (nm)	H (nm)	Absorption peak position (nm)	PL peak position (nm)
CS	1.65	1.96	591	605
<sup>a</sup> CSA1	1.65	2.05	626	648
<sup>a</sup> CSA2	1.65	2.15	627	649

<sup>a</sup> (CdSe<sub>x</sub>S<sub>1-x</sub>)<sub>n</sub> interfacial layers between CdSe and CdS, whereas x = 0.5, n = 4 for CSA1 QDs and x = 0.9–0.1, n = 5 for CSA2 QDs.

CdSe core, with x varies from 0.9, 0.7, 0.5, 0.3 and 0.1 respectively. Then one monolayer of CdS added to (CdSe<sub>x</sub>S<sub>1-x</sub>)<sub>5</sub> (x = 0.9–0.1) to synthesize CSA2 QDs.

### 2.3. Anode preparation

A thin and compact TiO<sub>2</sub> blocking layer was deposited on ultrasonically cleaned FTO glass substrates by hydrolysis of 0.50 mM TiCl<sub>4</sub> solution at 70 °C for 30 min. It was then annealed at 500 °C for 30 min under ambient atmosphere and left to cool down to room temperature. Double layer mesoporous films were prepared by tape casting a transparent layer of multiwall carbon nanotubes (MWCNT)-TiO<sub>2</sub> hybrid paste containing 0.010 wt% MWCNT (20 nm, 18 NR-T) [46] onto ultrasonically cleaned FTO glass substrates (sheet resistance 10 Ω/cm<sup>2</sup>). A drying process was followed for 15 min at ambient conditions and then placed on a hot plate for 6 min at 120 °C. Subsequently, a scattering layer of anatase TiO<sub>2</sub> nanoparticles (150–250 nm-sized, WER2-O) was applied on the above prepared transparent layer under the same conditions as described above. All photoanodes were then annealed at 500 °C for 30 min under ambient conditions. The thickness of as-fabricated photoanodes was measured by profilometer and an average value of 14–16 μm was found.

ZrO<sub>2</sub> films were prepared by using a commercial ZrO<sub>2</sub> nano-powder (Aldrich, particle size < 100 nm). A single layer of ZrO<sub>2</sub> film was deposited on FTO glass by tape casting. A drying process was followed for 10 min at ambient conditions and then placed on a hot plate for 6 min at 120 °C. Finally, ZrO<sub>2</sub> photoanodes were annealed in air at 500 °C for 30 min and cooled down to room temperature. The thickness of the ZrO<sub>2</sub> mesoporous film was in the range of 13–14 μm.

### 2.4. Electrophoretic deposition (EPD) of QDs on the TiO<sub>2</sub>-MWCNTs hybrid film and ZnS/SiO<sub>2</sub> coating

The as-prepared double layer mesoporous TiO<sub>2</sub>-MWCNTs hybrid photoanodes were vertically immersed in the QD toluene solution and the distance between two-electrodes was adjusted at 1 cm. A direct current bias of 200 V was applied for 120 min. Subsequently, the photoanodes were washed with toluene to remove the unbound QDs and finally dried with N<sub>2</sub> at room temperature. Prior to ZnS capping, a methanolic solution of cetyl-trimethyl ammonium bromide (CTAB) was used to exchange the surface native ligands. For details, 1 min dipping of photoanodes in CTAB and then washed in the corresponding solvent to remove the chemical residuals from the surface and then dried with N<sub>2</sub>, finally 1 min dipping in toluene and dried with N<sub>2</sub> for one SILAR cycle. This procedure was repeated three times, to remove most of the ligands. Subsequently, QDs sensitized TiO<sub>2</sub> mesoporous photoanodes were immersed in 0.01 M aqueous solution of TiCl<sub>4</sub> for 30 min at 40 °C and then sequentially rinsed with water and ethanol. In addition, one batch of QDs/ TiO<sub>2</sub> mesoporous photoanodes was prepared without TiCl<sub>4</sub> treatment to highlight the effect of TiCl<sub>4</sub>. A ZnS capping layer was formed through four SILAR cycles under the same conditions as for ligand exchanges. For ZnS deposition, Zn<sup>2+</sup> ions were deposited from 0.1 M methanolic solution of Zn (CH<sub>3</sub>COO)<sub>2</sub> 2H<sub>2</sub>O, whereas the S<sup>2-</sup> ions were deposited from 0.1 M mixed solution (1:1 methanol: water) of

Na<sub>2</sub>S. After ZnS capping, the SiO<sub>2</sub> coating was carried out by soaking in 0.01 M ethanolic solution of tetraethylorthosilicate for 2 h at 35 °C, then rinsed with ethanol and dried with N<sub>2</sub>.

### 2.5. Device fabrication

QDSCs were fabricated by sandwiching the QD sensitized TiO<sub>2</sub>-MWCNTs hybrid photoanode and the Cu<sub>2</sub>S counter electrode using a 25 μm thick plastic spacer. Polysulfide in H<sub>2</sub>O/methanol (1/1 v/v) (1 M Na<sub>2</sub>S, 1 M S and 0.1 M NaOH) was used as an electrolyte. The Cu<sub>2</sub>S counter electrode was fabricated by immersing the brass in HCl (30%) at 75 °C for 10 min. The HCl treated brass samples were subsequently immersed in polysulfide electrolyte (2 M Na<sub>2</sub>S, 2 M S and 0.2 M NaOH) solution for 10 min to yield Cu<sub>2</sub>S.

### 2.6. Characterization

TEM and HR-TEM images of QDs and QD-sensitized TiO<sub>2</sub> films were collected by using a JEOL 2100F TEM. XRD of purified QD films deposited on a silicon substrate (suitable for measuring XRD patterns in the 2θ range) was carried out using a Bruker D8 Advance diffractometer using a Cu K<sub>α</sub> radiation source (λ = 1.5418 Å). The UV–vis absorption spectra were recorded with a Cary 5000 UV–vis–NIR spectrophotometer (Varian) with a scan speed of 600 nm/min. Fluorescence spectra were acquired with a Fluorolog-3 system (Horiba Jobin Yvon). The PL lifetime and carrier transfer rate (electron/hole) were measured by using transient PL decay of QDs coupled with carrier scavengers (TiO<sub>2</sub> and polysulfide electrolyte) under the time-correlated single-photon counting (TCSPC) mode with a 444 nm laser. For the electron transfer rate measurements, QDs were deposited onto TiO<sub>2</sub> or ZrO<sub>2</sub> mesoporous films. The ZrO<sub>2</sub>/QDs film serves as a benchmark sample, in which the energy levels do not favour the electron/hole transfer from the QDs to ZrO<sub>2</sub>. The electron transfer rate was calculated from the difference in the electron lifetime values of QDs with TiO<sub>2</sub> or ZrO<sub>2</sub> mesoporous films. Similarly, the hole transfer rate was monitored by immersing the ZrO<sub>2</sub>/QDs film into the polysulfide electrolyte as a hole scavenger.

The current-voltage (*I*-*V*) and transient photovoltage decay measurements were carried out using a compact solar simulator class AAA (Sciencetech SLB-300A) under one sun simulated sunlight (1 sun = AM 1.5G, 100 mW/cm<sup>2</sup>), calibrated with a silicon reference cell. External quantum efficiency (EQE) spectra of QDSCs were recorded using an IQE200B system (Newport Corporation) with a chopper speed of 4 Hz.

### 2.7. Theoretical calculations

Theoretical wave functions for electrons and holes were calculated by solving the stationary Schrödinger wave equation in spherical geometry, in which we used the bulk values for the effective masses of electrons ( $m_e^*$ ) and holes ( $m_h^*$ ), namely  $m_e^* = 0.44 m_e$  and  $m_h^* = 0.13 m_e$  for CdSe [47], and  $m_e^* = 0.2 m_e$  and  $m_h^* = 0.7 m_e$  for CdS [48], where  $m_e$  is the electron mass at rest in vacuum. The potentials for electrons and holes as a function of position were approximated as the lowest unoccupied molecular orbital (LUMO) and highest occupied molecular orbital (HOMO) levels, respectively, for the bulk materials. For CdSe, these levels are –3.71 and – 5.81 eV, respectively, while for CdS they are – 3.3 and – 5.8 eV, respectively. For the alloyed CdSe<sub>x</sub>S<sub>1-x</sub> interfacial layers, we used weighted averages (x for Se and 1-x for S, x = 0.5) of the above quantities. Outside the QD, the potentials were set as 0 and – 9.8 eV for electrons and holes, respectively. The interaction between electrons and holes was neglected in the calculations.

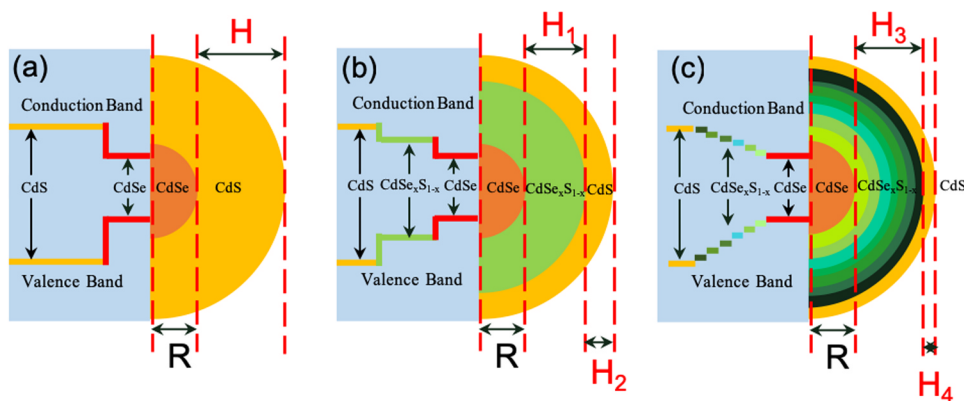


**Fig. 1.** Schematic illustration of internal interfacial structures and carrier confinement potentials of QDs: (a) CdSe/(CdS)<sub>6</sub>, ( $R = 1.65$  nm,  $H = 1.96$  nm) (CS QDs); (b) CdSe/(CdSe<sub>*x*</sub>S<sub>*1-x*</sub>)<sub>4</sub>/(CdS)<sub>2</sub> ( $x = 0.5$  for all monolayers,  $R = 1.65$  nm,  $H_1 = 1.39$  nm,  $H_2 = 0.66$  nm) (CSA1 QDs); and (c) CdSe/(CdSe<sub>*x*</sub>S<sub>*1-x*</sub>)<sub>5</sub>/(CdS)<sub>1</sub> ( $x = 0.9-0.1$ ,  $R = 1.65$  nm,  $H_3 = 0.82$  nm,  $H_4 = 0.33$  nm) (CSA2 QDs).  $R$  is Radius of CdSe QDs and  $H$  is the shell thickness.

### 3. Results and discussion

#### 3.1. Synthesis and structure of colloidal core/shell QDs

CdSe core QDs were first synthesized via a hot injection approach, as reported elsewhere [49]. Subsequently, a CdS shell was overgrown by SILAR at 240 °C under N<sub>2</sub> flow (see Experimental Section) to form a CS QDs. To broaden the absorption of the CS QDs and reduce the interfacial potential at the sharp interface between CdSe core and CdS shell, we synthesized four monolayers of interfacial CdSe<sub>0.5</sub>S<sub>0.5</sub> alloyed shell over the CdSe core QDs, then two additional monolayers of CdS were grown on the alloyed shell to form CSA1 QDs. Graded alloyed CSA2 QDs were synthesized by tailoring the Se:S ratio during in situ growth of each CdSe<sub>*x*</sub>S<sub>*1-x*</sub> ( $x = 0.9-0.1$ ) interfacial layer over the CdSe core QDs. The diameter of the starting CdSe core QDs is around  $3.30 \pm 0.29$  nm. The increased size of QDs after CdS shell growth was confirmed by TEM imaging [see Fig. 2(a)-(c)]. The average CdSe core size and (CdS)<sub>6</sub>, alloyed (CdSe<sub>0.5</sub>S<sub>0.5</sub>)<sub>4</sub>/(CdS)<sub>2</sub> and graded alloyed (CdSe<sub>*x*</sub>S<sub>*1-x*</sub>)<sub>5</sub>/(CdS)<sub>1</sub> ( $x = 0.9-0.1$ ) shell thickness ( $H$ ) are reported in Table 1. In brief, after growing six monolayers of CdS, the diameter of the as-synthesized CS QDs is  $7.2 \pm 0.5$  nm ( $H = 1.96$  nm), whereas for alloyed CSA1 and graded alloyed CSA2 QDs, with the growth of four interfacial layers of CdSe<sub>*x*</sub>S<sub>*1-x*</sub> ( $x = 0.5$ )/two monolayers of CdS, and five interfacial layers of CdSe<sub>*x*</sub>S<sub>*1-x*</sub> ( $x = 0.9-0.1$ )/ one monolayer of CdS, the final diameter reaches  $7.4 \pm 0.7$  nm ( $H = 2.05$  nm) and  $7.6 \pm 1.3$  nm ( $H = 2.15$  nm) respectively. The size distributions of as-synthesized CS, CSA1 and CSA2 QDs are shown in Fig. 1S. The high crystallinity with lattice fringes of each QD is clearly visible in the HRTEM image [inset Fig. 2(a), (b) and (c)]. The calculated lattice parameter of CS, CSA1 and CSA2 QDs shown in Fig. 2(a), (b) and (c) are = 3.33 Å, 3.60 Å, and 3.61 Å corresponds to the (0 0 2), (1 0 0) and (1 0 1) lattice spacing of the Wurtzite (WZ) crystal structure of studied QDs respectively. These findings are consistent with the SAED pattern and XRD of the respective QDs. The homogeneous dispersion of the CSA2 QDs (yellow dotted circles) on the surface of the TiO<sub>2</sub> mesoporous film without any aggregation during the deposition of QDs via EPD is confirmed in Fig. 2(d) and is consistent with optical properties measurements of as-synthesized QDs and QDs deposited onto the TiO<sub>2</sub> mesoporous film.

Fig. 2(e) displays the XRD patterns of colloidal CS, CSA1 and CSA2 QDs. The peak positions of the XRD patterns of CS QDs confirmed the hexagonal WZ crystal structure of CS QDs, which is mainly attributed to the dominance of the thick CdS shell (six SILAR cycles) over the CdSe core QDs. These findings are consistent with our previous work [31]. On the other hand, in the case of CSA1 and CSA2 QDs, the slight shifting of the XRD peak positions as well as the combined reflection of WZ crystal structure of CdS and WZ crystal structure of CdSe confirm the formation of alloyed CSA1 and graded alloyed CSA2 WZ structured QDs. The SAED patterns of CS QD are shown in Fig. 2(f) and tabulated (002), (110), (103) and (112) planes of WZ phase. Similarly, SAED

patterns of alloyed CSA1 and graded alloyed CSA2 QDs are shown in Fig. 2(g-h) and tabulated (111), (211), (220), (311) and (111), (211), (220), (310), (311) planes also of WZ phase respectively. These findings are consistent with the XRD analysis of the corresponding QDs.

The optical properties of as-synthesized CS, CSA1 and CSA2 QDs in toluene are shown in Fig. 3 and the calculated optical parameters of the corresponding QDs are reported in Table 1. The first-excitonic absorption peak for CS QDs is observed around 591 nm [Fig. 3(a)]. With the incorporation of CdSe<sub>*x*</sub>S<sub>*1-x*</sub> interfacial layers, the first-excitonic absorption peak systematically shifts toward longer wavelength with extended absorption spectra. In brief, alloyed CSA1 QDs show first-excitonic absorption peak near 626 nm, with absorption spectra extended from 300 to 670 nm. Similarly, CSA2 QDs exhibit a first-excitonic absorption peak around 627 nm and absorption spectra extended from 300 to 700 nm [Fig. 3(a)]. This significant broadening of the absorption spectra in case of CSA2 and CSA1 QDs with respect to CS QDs having comparable shell thickness highlights the benefits of alloyed interfacial layers at the core/shell sharp interface of CS QDs. Hence CSA1 and CSA2 QDs can harvest a higher number of photons, leading to higher PCE of the QDSCs based on these QDs with respect of the CS QDs (see photovoltaic measurements section).

The PL spectra of as-synthesized CS, CSA1 and CSA2 QDs dispersed in toluene are shown in Fig. 3(b). The PL peak position of the CS QDs at 605 nm shifts significantly to longer wavelength (~ 650 nm) after the addition of CdSe<sub>*x*</sub>S<sub>*1-x*</sub> interfacial layers. Further modification of the CdSe<sub>*x*</sub>S<sub>*1-x*</sub> interfacial layers (for CSA2 QDs) does not lead to any significant change in the PL peak position (649 nm) with respect to CSA1 (PL- 648 nm) as we observed in the absorption spectra of the corresponding QDs.

This redshift (~ 45 nm) in the PL peak position of CSA2 and CSA1 QDs system with respect to the reference CS QDs of comparable size, is due to enhanced carrier (both electron and hole) delocalization into the shell region (detailed discussion in the following Section) and the increased concentration of CdSe [50]. However, in the reference CS QDs, only electrons are delocalized into the shell region, while holes are confined into the core [23,44]. These findings are consistent with UV-visible measurements and further supported by PL lifetime measurements and theoretical wave function calculations of corresponding QDs systems.

The half width half maxima (HWHM) of absorption peak and full-width half maxima (FWHM) of PL peak of CS, CSA1 and CSA2 QDs were calculated by using Gaussian multiple peaks fitting approach. The values of HWHM of the absorption peak of CS, CSA1 and CSA2 QDs are 0.45, 0.49 and 0.47 eV respectively. Similarly, the values of FWHM of PL peak of CS, CSA1 and CSA2 QDs are 0.971, 0.108 and 0.114 eV respectively. The difference in the values of HWHM and FWHM of CSA1 and CSA2 QDs is very small. This slight broader PL peak of CSA2 QDs compared to CSA1 QDs may be contributed from instrumental error.

In addition, the stability of CS, CSA1 and CSA2 QDs is highlighted in PL measurements of as-synthesized QDs in toluene and deposited on the

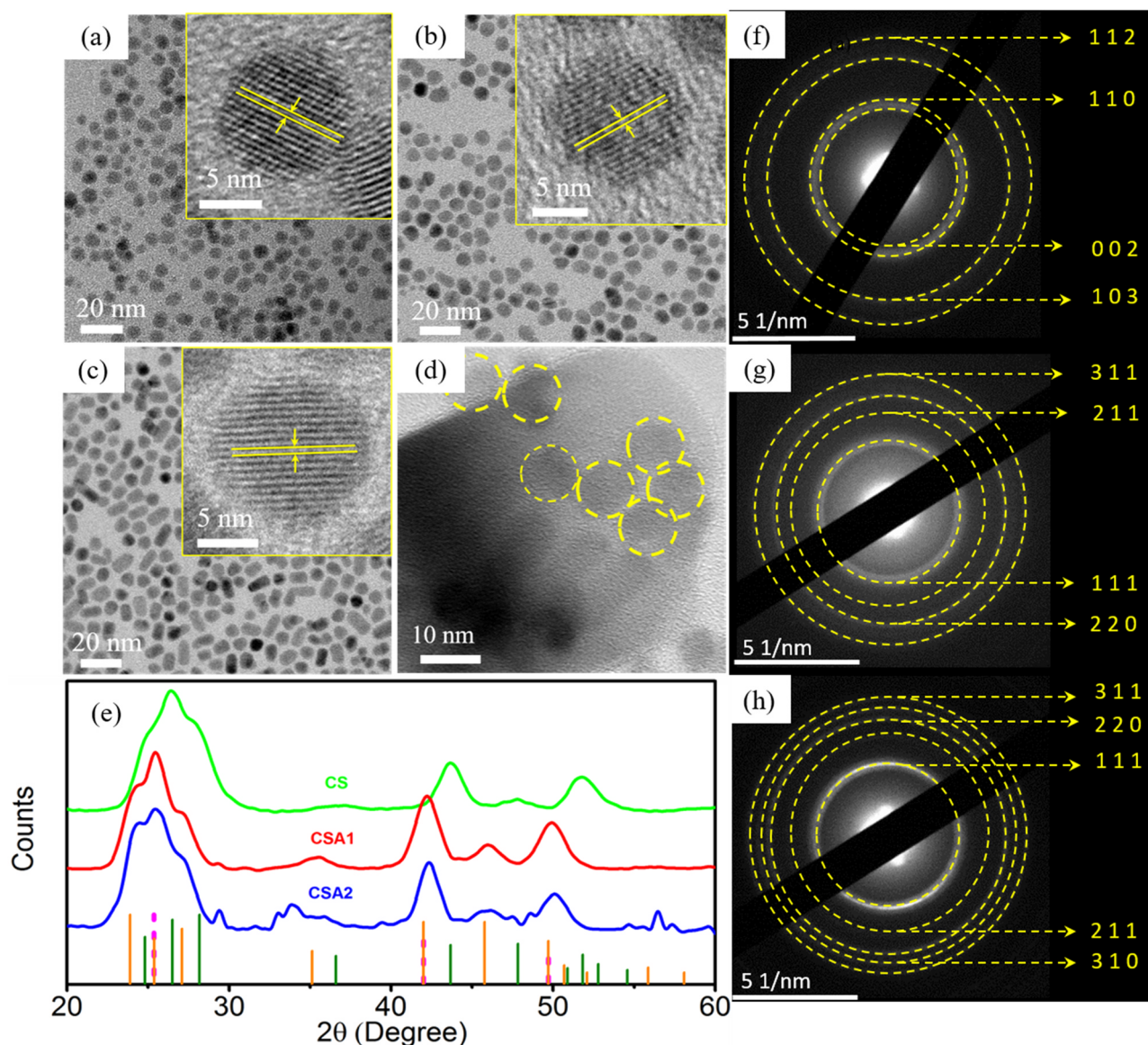


**Fig. 2.** TEM images of: (a) as-synthesized CdSe/(CdSe)<sub>6</sub> QDs (CS); after growth of (CdSe<sub>x</sub>S<sub>1-x</sub>)<sub>n</sub> interfacial layers between CdSe and CdS: (b)  $x = 0.5$ ,  $n = 4$  for CSA1 QDs; (c)  $x = 0.9-0.1$ ,  $n = 5$  for CSA2 QDs. Inset of (a)–(c) showing the HR-TEM image of corresponding QDs. (d). HR-TEM image of CSA2 QDs sensitized TiO<sub>2</sub> film, dotted yellow circles highlight the presence of QDs. (e) XRD patterns of CS QDs (green line), CSA1 QDs (red line) and CSA2 QDs (blue line). The Joint Committee on Powder Diffraction Standards (JCPDS) card files for CdSe (00190191, pink dashed for ZB and 08–459, yellow for WZ) and CdS (01-077-2306, green for WZ) are shown for identification. SAED pattern: (f) CS QDs; (g) CSA1 QDs; and (h) CSA2 QDs.

surface of mesoporous TiO<sub>2</sub> film after 2 h EPD. We found that the PL peak position and PL shape remain unchanged after QDs deposited on TiO<sub>2</sub> with respect to QDs in toluene [see Fig. 3(c) and Fig. 2S(a)–(b)].

### 3.2. Charge dynamics of QDs coupled with carrier scavengers

The absorption of photons by the QDs generates an exciton that dissociates at two interfaces: the QDs/metal oxide and the QDs/redox couple electrolyte. The optimized band alignment of the conduction band (CB) of TiO<sub>2</sub> with the CB of QDs leads to efficient electron injection from the QDs to TiO<sub>2</sub> and reaches the cathode through FTO and the external load. The hole in the valence band (VB) of the QDs is transferred to the polysulfide electrolyte. Therefore, understanding of carrier dynamics is crucial to improve device performance. We used transient PL spectroscopy to understand the carrier dynamics of QDs after coupling with carrier scavengers. The electron lifetime ( $\tau$ ) and carrier transfer rate of QDs with carrier scavengers (mesoporous TiO<sub>2</sub> film and polysulfide electrolyte) were measured under the excitation

wavelength  $\lambda = 444$  nm. All the PL decay curves were well fitted by an exponential decay. The intensity-weighted average lifetime ( $\langle \tau \rangle$ ) is calculated by using the following equation:

$$\langle \tau \rangle = \sum \frac{a_i \tau_i^2}{a_i \tau_i} \quad (1)$$

Where  $a_i$  ( $i = 1, 2, 3$ ) are the fitting coefficients and  $\tau_i$  ( $i = 1, 2, 3$ ) are the characteristic lifetimes of the PL decay, respectively.

For all types of QDs, the PL decay is faster in the case of QDs with TiO<sub>2</sub> and electrolyte, compared to QDs with ZrO<sub>2</sub>, which confirms that charge transfer is more efficient towards carrier scavengers (TiO<sub>2</sub> and electrolyte) than to ZrO<sub>2</sub> [Fig. 4(a)–(c)]. We calculated the  $\tau$  of QDs of different shell structures and compositions with the same CdSe core size by measuring the PL intensity decay of QDs anchored to the TiO<sub>2</sub> mesoporous film [see Fig. S3(b)]. The variation of the  $\tau$  of core/shell QDs with different shell structures and compositions is shown in Fig. 4(d) and the corresponding values are reported in Table 2. The highest  $\tau$  of

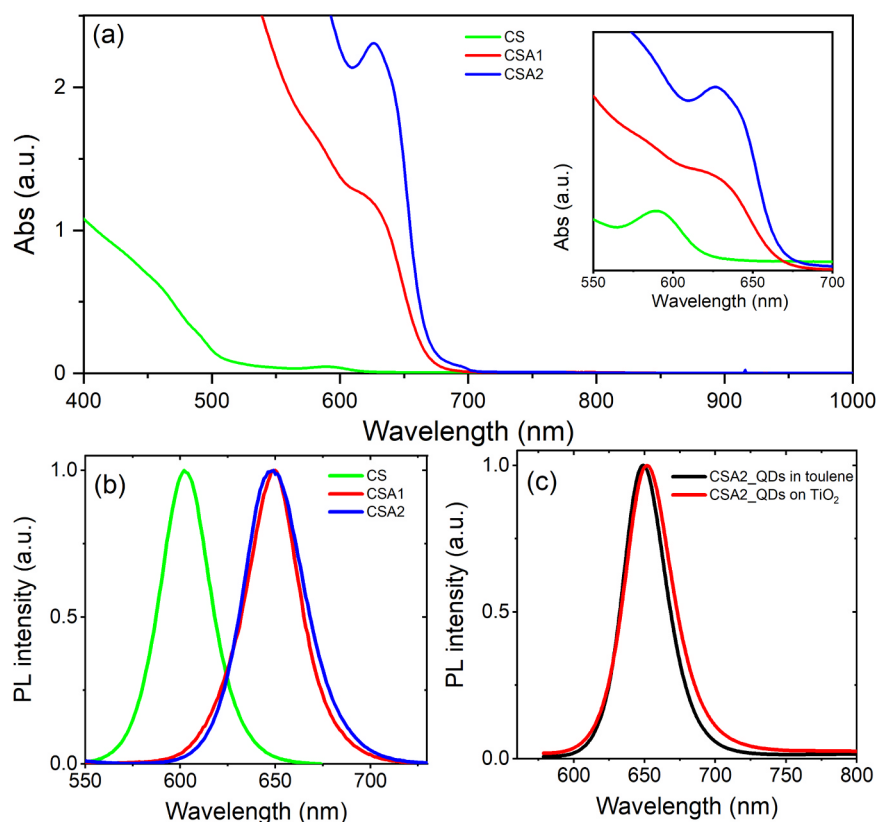


**Fig. 3.** Optical measurements: (a) UV-vis absorption spectra of as-synthesized CS QDs in toluene before and after growth of  $(\text{CdSe}_x\text{S}_{1-x})_n$  interfacial layers between CdSe and CdS, whereas  $x = 0.5$ ,  $n = 4$  for CSA1 QDs and  $x = 0.9-0.1$ ,  $n = 5$  for CSA2 QDs. The inset shows the magnified absorption spectra of the corresponding QDs in toluene, where the first excitonic absorption peaks are clearly visible; (b) PL spectra of corresponding QDs in toluene; (c) PL spectra of the CSA2 QDs in toluene and QDs deposited on  $\text{TiO}_2$  mesoporous film via EPD.

$29 \pm 0.4$  ns is reported for CS QDs. This is mainly attributed to the confinement of the holes into the core region and leakage of the electrons into the shell region of CS QDs. On the other hand,  $\tau$  values are decreased to  $24 \pm 0.5$  ns and  $14 \pm 0.4$  ns for CSA1 and CSA2 QDs respectively. The presence of interfacial layers  $(\text{CdSe}_x\text{S}_{1-x})_n$  ( $x = 0.5$ ,  $n = 4$ ) for CSA1 and ( $x = 0.9-0.1$ ,  $n = 5$ ) for CSA2 QDs leads to the formation of favorable stepwise band alignment between the CdSe core and alloyed shell as shown in Fig. 1(b) – (c). Due to this favorable band alignment of CSA1 and CSA2 QDs, both electrons and holes leak into the shell region, whereas in CS QDs only electrons leak into the shell region. The possibility of holes leaking in the shell region induces greater e-h overlap in CSA1 and CSA2 QDs, leading to fast e-h recombination and reducing the overall  $\tau$  values [51]. The lowest value of  $\tau$  is obtained for the CSA2 QDs due to the modification of the interfacial layer band of CSA1 QDs into graded interfacial layer bands in CSA2 QDs as shown in Fig. 1(c). This favorable stepwise band alignment of graded alloyed CSA2 QDs leads to faster hole leakage into the shell region as compared to CSA1 QDs, which is consistent with the obtained  $\tau$  values. A similar trend for  $\tau$  was observed for the QDs coupled with  $\text{ZrO}_2$  film. The trend is shown in Fig. S3(c) and corresponding values are reported in Table 2. This enhanced e-h overlap in case of CSA1 and CSA2 QDs system with respect to the reference CS QDs system is also confirmed by theoretical calculations, as discussed below.

We also investigated the effects of the incorporation of  $\text{CdSe}_x\text{S}_{1-x}$  interfacial layers between CdSe core and CdS shell of core/shell QDs on carrier dynamics by coupling the QDs with carrier scavengers. In this measurement, a mesoporous  $\text{TiO}_2$  metal oxide film is used as electron scavenger, while polysulfide (1 M  $\text{Na}_2\text{S}$ , 1 M S and 0.1 M NaOH) in  $\text{H}_2\text{O}$ /methanol (1/1 v/v) is used as a hole scavenger. The CS QDs system is considered as the reference. In previous work, we ruled out the possibility of energy transfer from QDs to carrier scavengers [39], because there is no spectral overlap between the PL of QDs and absorption of carrier scavengers ( $\text{TiO}_2$  and polysulfide electrolyte) [52]. Hence this faster PL decay of the QDs system coupled with carrier scavengers ( $\text{TiO}_2$  and polysulfide electrolyte) than QDs with  $\text{ZrO}_2$  is

mainly attributed to the possibility of electron transfer from the CB of QDs to CB of  $\text{TiO}_2$  and hole transfer from VB of QDs to the polysulfide electrolyte (Fig. S3).

The carrier lifetime values for all QDs with the  $\text{TiO}_2$  mesoporous film (electron scavenger) and polysulfide electrolyte (hole scavenger) are shorter than the QDs with  $\text{ZrO}_2$  mesoporous film as shown in Fig. 4 (the corresponding values are reported in Table 2). From the differences in the carrier lifetime values, we calculated the carrier transport rate ( $K_{\text{et}}$  or  $K_{\text{ht}}$ ) by using the following equation:

$$K_{\text{et or ht}} = \frac{1}{\langle \tau \rangle_{\text{QDs}/e(\text{TiO}_2) \text{ or } h(\text{electrolyte})}} - \frac{1}{\langle \tau \rangle_{\text{QDs}/(\text{ZrO}_2)}} \quad (2)$$

Where  $\langle \tau \rangle_{\text{QDs}/e(\text{TiO}_2) \text{ or } h(\text{electrolyte})}$  and  $\langle \tau \rangle_{\text{QDs}/\text{ZrO}_2}$  are the average lifetimes of the QDs with carrier scavengers and QDs with  $\text{ZrO}_2$  respectively.

The calculated electron transport rate ( $K_{\text{et}}$ ) of  $0.6 \pm 0.1 \times 10^7/\text{s}$  for CS QDs [see Fig. 4(e)], is lower than the  $K_{\text{et}}$  of both CSA1 ( $2.2 \pm 0.1 \times 10^7/\text{s}$ ) and CSA2 QDs ( $2.6 \pm 0.1 \times 10^7/\text{s}$ ). This can be attributed to high interfacial potential, less degree of carrier delocalization (see Section 3.3) and presence of defect states at the sharp interface of CdSe core and CdS shell of the reference CS QDs system. In brief, for CSA1 QDs,  $K_{\text{et}}$  increases significantly to  $2.2 \pm 0.1 \times 10^7/\text{s}$ , which is 3 times higher than the  $K_{\text{et}}$  of CS QDs [see Fig. 4(e) and corresponding value reported in Table 2], although the driving force of electron injection from the CB of CSA1 QDs into CB of  $\text{TiO}_2$  is slightly lower than the reference CS QDs. This considerably higher value of  $K_{\text{et}}$  ( $2.2 \pm 0.1 \times 10^7/\text{s}$ ) is mainly attributed to the dominance of the effect of favorable electronic band alignment of the CdSe core with  $\text{CdSe}_x\text{S}_{1-x}$  interfacial layers and CdS shells [see Fig. 1(b)], which reduces the overall interfacial potential and defect states and enhances the carrier delocalization into the shell region, over the slight less driving force for the electron injection, hence accelerates the electron injection from CB of QDs to CB of  $\text{TiO}_2$ . This  $K_{\text{et}}$  value is further enhanced to  $2.6 \pm 0.1 \times 10^7/\text{s}$  by tailoring the Se:S molar ratios during in situ growth of each interfacial layer of CSA2 QDs system. This leads to a

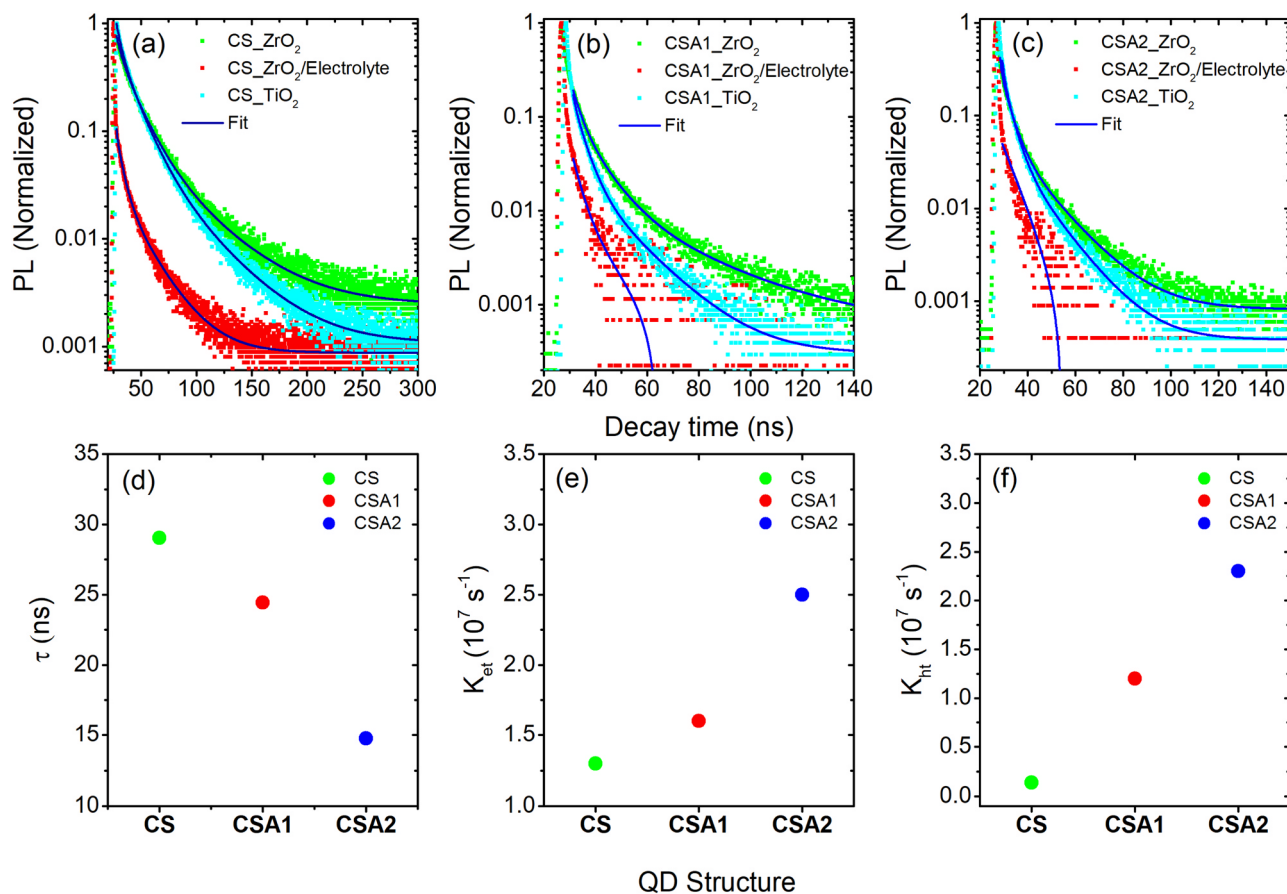


**Fig. 4.** Transient PL curves of core/shell QDs deposited onto ZrO<sub>2</sub> mesoporous film, ZrO<sub>2</sub> film with polysulfide electrolyte, and TiO<sub>2</sub> mesoporous film: (a) CS QDs; (b) CSA1 QDs and (c) CSA2 QDs. The excitation wavelength is  $\lambda_{\text{ex}} = 444$  nm. Calculated parameters from the comparative study of core/shell QDs with different shell structure and compositions: (d) Electron lifetime; (e) Electron transfer rate; and (f) Hole transfer rate.

further reduction of the overall interfacial potential by improved favorable stepwise band alignment of graded alloyed interfacial layers between CdSe core and CdS shell QDs, as shown in Fig. 1(c) and enhanced degree of carrier delocalization into the shell region (see Section 3.3).

Similarly, the hole transport rate ( $K_{\text{ht}}$ ) from VB of QDs to the electrolyte for all QDs systems follows the same trend as  $K_{\text{et}}$  shown in Fig. 4(f) and the corresponding values are reported in Table 2.  $K_{\text{ht}}$  is lowest for CS QDs ( $0.14 \pm 0.3 \times 10^7/\text{s}$ ) and highest for CSA2 QDs ( $2.3 \pm 0.5 \times 10^7/\text{s}$ ). This observation can be attributed to the reduced interfacial potential for hole transfer by incorporation of alloyed and graded alloyed CdSe<sub>x</sub>S<sub>1-x</sub> interfacial layers between CdSe core and CdS shell. Thus, the transient PL decay measurements demonstrated that the carrier transport (both electrons and holes) can be modified by engineering the interfacial layers between CdSe core and CdS shell of CS QDs system.

### 3.3. Theoretical electron-hole wave function calculations

To describe theoretically the optoelectronic properties of CS, CSA1 and CSA2 QDs, we calculated the electron ( $\psi_e(r)$ ) and hole ( $\psi_h(r)$ ) wave functions by solving the stationary Schrödinger wave equation in spherical geometry [48]. The calculation details are reported in the Experimental Section. The variation of calculated spatial probability distribution ( $\rho(r)$ ) of  $\psi_e(r)$  and  $\psi_h(r)$  as a function of QDs radius ( $r$  (nm)) for all QDs systems is shown in Fig. 5(a)–(c).

A systematic comparison of  $\rho(r)$  of  $\psi_e(r)$  and  $\psi_h(r)$  for all QDs shows the leakage of the electrons into the shell region, while the holes confined in the CdSe core confirmed the possible formation of a quasi-type II band alignment [23,33,53,54]. The calculated e-h spatial overlap area (%) of  $\psi_e(r)$  and  $\psi_h(r)$ , is plotted as a function of QDs structure is shown in Fig. 5(d) and the corresponding values are reported in Table S1. The lowest e-h spatial overlap area (%) obtained is 64% for CS QDs, which increases to 67% for CSA1 and 72% for CSA2 QDs. This slight increase in e-h spatial overlap area (%) with the addition CdSe<sub>x</sub>S<sub>1-x</sub> interfacial layers between CdSe core and CdS shell in CSA1 ( $x = 0.5$ ) or

**Table 2**

Calculated electron lifetime ( $\tau$ ), electron transfer rate ( $K_{\text{et}}$ ) and hole transfer rate ( $K_{\text{ht}}$ ) from transient PL spectroscopy measurements for the core/shell QDs of different shell structure and compositions deposited on mesoporous ZrO<sub>2</sub> film and carrier scavengers (mesoporous TiO<sub>2</sub> film and polysulfide electrolyte).

QDs structure	R (nm)	H (nm)	Lifetime with TiO <sub>2</sub> (ns)	Lifetime with ZrO <sub>2</sub> (ns)	$K_{\text{et}}$ ( $10^7/\text{s}$ )	$K_{\text{ht}}$ ( $10^7/\text{s}$ )
CS	1.65	1.96	$29 \pm 0.4$	$48 \pm 0.6$	$0.6 \pm 0.1$	$0.14 \pm 0.2$
<sup>a</sup> CSA1	1.65	2.05	$24 \pm 0.5$	$39 \pm 0.1$	$2.2 \pm 0.1$	$1.3 \pm 0.3$
<sup>a</sup> CSA2	1.65	2.15	$14 \pm 0.8$	$23 \pm 0.3$	$2.6 \pm 0.1$	$2.3 \pm 0.5$

<sup>a</sup> (CdSe<sub>x</sub>S<sub>1-x</sub>)<sub>n</sub> interfacial layers between CdSe and CdS, whereas  $x = 0.5$ ,  $n = 4$  for CSA1 QDs and  $x = 0.9\text{--}0.1$ ,  $n = 5$  for CSA2 QDs.

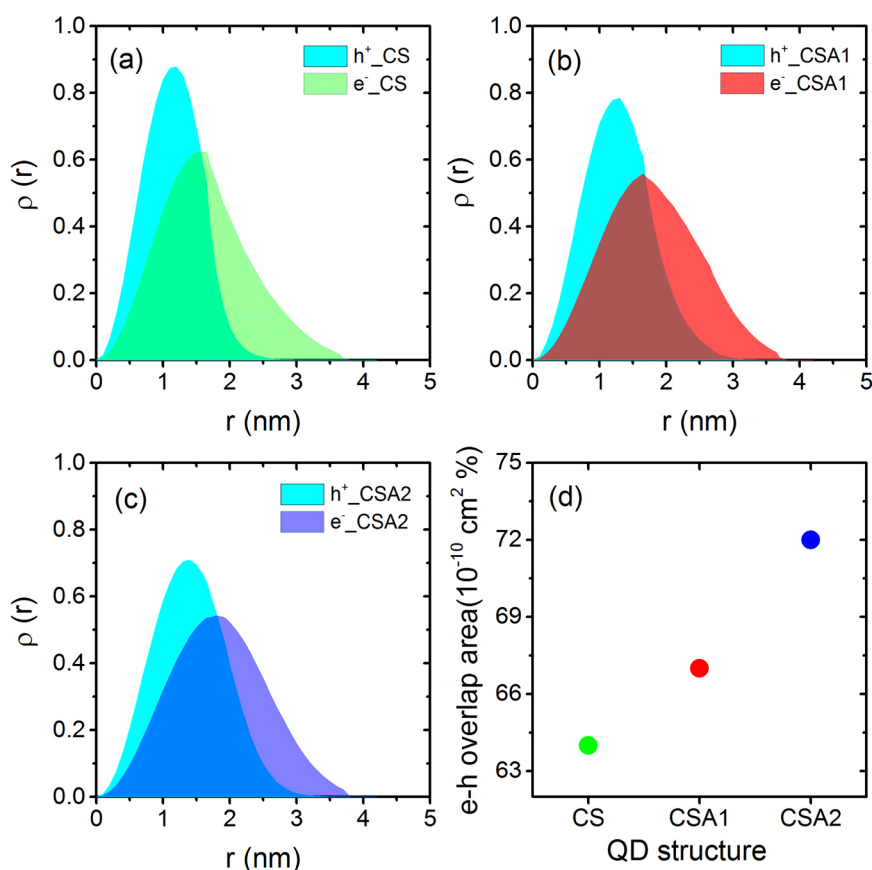


Fig. 5. Comparison of spatial probability distribution value  $\rho(r)$  of the electron and hole as a function of QDs radius  $r$  (nm) for core/shell and alloyed core/shell QDs: (a) CS (cyan for hole and green for electron); (b) CSA1 (cyan for hole and red for electron); (c) CSA2 (cyan for hole and blue for electron); and (d) electron-hole spatial overlap area (%) variation with respect to QDs structure (green circle: CS QDs; red circle: CSA1 QDs and blue circle: CSA2 QDs).

CSA2 ( $x = 0.9-0.1$ ) QDs with respect to CS QDs is due to favorable stepwise band alignment of CSA1 and CSA2 QDs [see Fig. 1(b) and (c)] [48].

This favorable stepwise band alignment reduces the overall interfacial barrier potential that could slow down or even block hole transfer from the CdSe core into the shell region [see Fig. 1(a)-(c)]. So, the probability of the holes to leak into the shell region for CSA1 and CSA2 QDs is higher than the holes in CS QDs. The increased e-h spatial overlap area (%) in the case of CSA1 and CSA2 QDs, enhances the e-h recombination probability and reduces the overall  $\tau$ . These measurements are consistent with carrier dynamics studies of the respective QDs reported in the previous section [see Fig. 4(d)].

### 3.4. Photovoltaic performance

As a proof-of-concept, we fabricated QDSCs based on QDs sensitized TiO<sub>2</sub>-MWCNTs hybrid mesoporous film photoanode. The photocurrent density-voltage ( $J$ - $V$ ) curves of QDSCs based on core/shell QDs of different structures under one sun simulated sunlight (AM 1.5G, 100 mW/cm<sup>2</sup>) are shown in Fig. 6(a) and the corresponding calculated PV parameters are reported in Table 2. The QDSC based on CS QDs show a PCE of 3.08%, short circuit current density ( $J_{sc}$ ) of 9.52 mA/cm<sup>2</sup>, open circuit voltage ( $V_{oc}$ ) of 565 mV and fill factor ( $FF$ ) of 57%. This PV performance is significantly enhanced by engineering the sharp interface between CdSe core and CdS shell of CS QDs system with the incorporation of CdSe<sub>x</sub>S<sub>1-x</sub> ( $x = 0.5$ ) interfacial layers (CSA1 QDs), while maintaining the same structure of the CdSe core, as shown in schematic Fig. 1(b).

We find that  $J_{sc}$  increases from 9.52 to 16.72 mA/cm<sup>2</sup> and  $V_{oc}$  from 565 to 576 mV, leading to a PCE of 5.52%. The presence of (CdSe<sub>x</sub>S<sub>1-x</sub>)<sub>n</sub> ( $x = 0.5$ ,  $n = 4$ ) alloyed interfacial layers between the CdS shell and the CdSe core reduce the overall interfacial potential and defects states at the CdSe/CdS core/shell sharp interface. This significantly enhances the

electron injection from the CB of the QDs to the CB of TiO<sub>2</sub> ( $K_{et}$ ) and the hole transfer ( $K_{ht}$ ) from the VB of the CSA1 QDs to the polysulfide electrolyte, as demonstrated in transient PL decay measurements [see Fig. 4 and Table 2]. The PCE of QDSC based CSA2 QDs system attains values of 7.14% (see Table 3), which is 29% higher than the QDSC based on CSA1 QDs and is also higher than the PCE reported in the literature for liquid junction QDSCs of similar configuration based on core/thin shell QDs (more details reported in 1.1S Section, supporting information). This is mainly attributed to a further reduction in the overall interfacial potential by improved favorable stepwise band alignment [see Fig. 1(c)] and broadening of the absorption spectrum towards longer wavelengths [see Fig. 3(a)] of the CSA2 QDs. These results are further supported by EQE and transient photovoltage decay measurements of the QDSCs.

Fig. 6(b) displays the systematic comparison of the EQE spectra of QDSCs based on CS, CSA1 and CSA2 QDs as a function of wavelength. The EQE of the device depends on the light harvesting efficiency ( $\eta_{LHE}$ ), charge transfer efficiency ( $\eta_{ct}$ ) and charge-collection efficiency ( $\eta_{cc}$ ) [54]. The QDSC based on CSA2 QDs shows broader EQE spectra towards longer wavelengths ( $\sim 650-700$  nm) with respect to QDSCs based on CSA1 and reference CS QDs. This is mainly attributed to better  $\eta_{LHE}$  and  $\eta_{ct}$  properties of CSA2 QDs as compared to CSA1 and CS QDs, which is confirmed by UV-visible absorption and carrier dynamic measurements of QDs. At 500 nm, the EQE (%) values of QDSCs follow the trend CSA2 QDs ( $\sim 80\%$ ) > CSA1 QDs ( $\sim 67\%$ ) > CS QDs ( $\sim 40\%$ ). The trend of EQE (%) measurements is consistent with the PV results of the three QDSCs.

The variation of the PV parameters:  $J_{sc}$  (mA/cm<sup>2</sup>); PCE (%);  $V_{oc}$  (V); and  $FF$  (%) with the QDs shell structure and composition is shown in Fig. 6(e)-(f). QDSC based on CSA1 QDs exhibit better PV parameters compared to QDSCs based on CS QDs. The performance of the QDSC can be further improved by using CSA2 QDs as a light harvester [see Fig. 6(e)-(f) and corresponding values reported in Table 3]. A

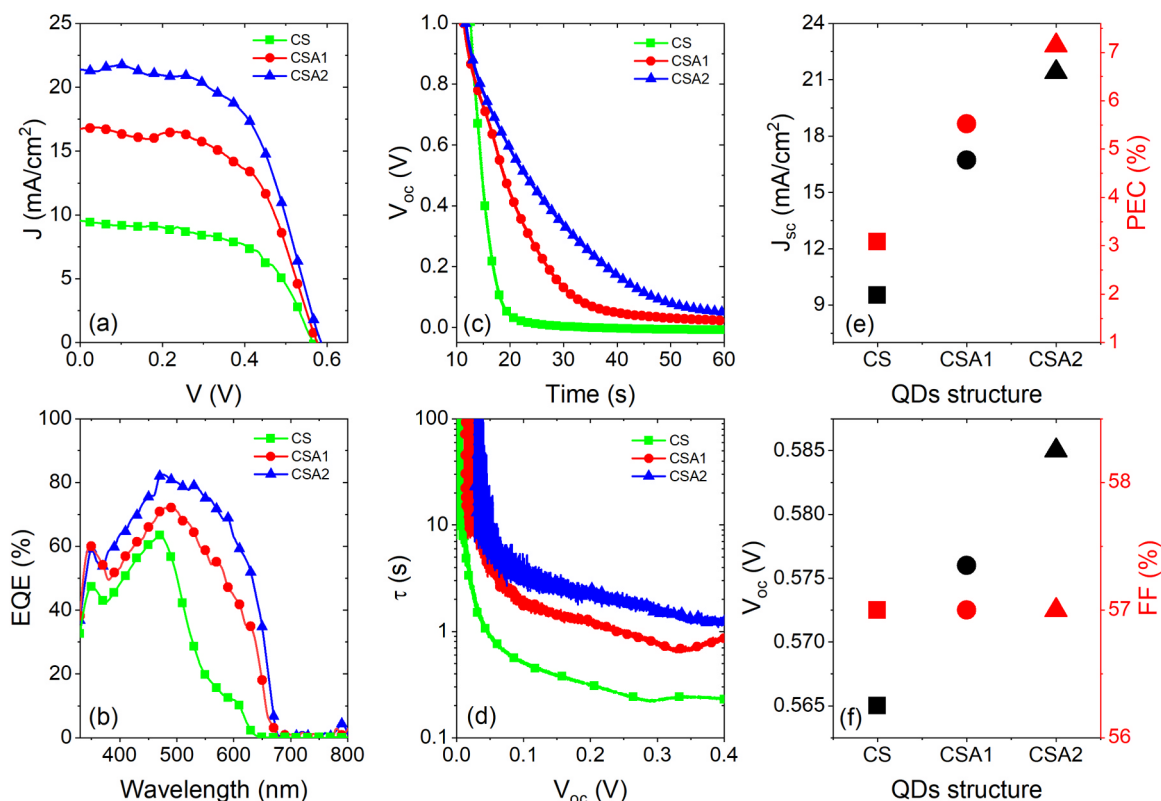


**Fig. 6.** (a) Comparison of current density versus voltage curves of CS QDs (green squares), CSA1 QDs (red circles) and CSA2 QDs (blue up-triangular) based QDSCs under one sun irradiation (AM 1.5G,  $100 \text{ mW/cm}^2$ ); (b) EQE (%) of the corresponding QDSCs. Transient photovoltage decay measurements: (c)  $V_{oc}$  decay as the function of time; (d) electron lifetime ( $\tau$ ) as a function of  $V_{oc}$ , calculated from  $V_{oc}$  decay measurements. Photovoltaic parameters variations of QDSCs with QDs structure: (e)  $J_{sc}$  ( $\text{mA/cm}^2$ ) (black color, left) and PCE (%) (red color, right); (f)  $V_{oc}$  (V) (black color, left) and FF (%) (red color, right).

**Table 3**

Comparison of the photovoltaic parameters calculated from  $J$ - $V$  measurements of QDSCs based on CS, CSA1 and CSA2 QDs as light harvesters.

QDs structure	H (nm)	$J_{sc}$ ( $\text{mA/cm}^2$ )	$V_{oc}$ (mV)	FF (%)	PCE (%)
CS	1.96	9.52	565	57	3.08
<sup>a</sup> CSA1	2.05	16.72	576	57	5.52
<sup>a</sup> CSA2	2.15	21.39	585	57	7.14

<sup>a</sup>  $(\text{CdSe}_x\text{S}_{1-x})_n$  interfacial layers between CdSe and CdS, whereas  $x = 0.5$ ,  $n = 4$  for CSA1 QDs and  $x = 0.9$ – $0.1$ ,  $n = 5$  for CSA2 QDs.

systematic comparison of the PV performance of QDSCs based on the CS, CSA1 and CSA2 QDs demonstrates that this difference is due to the different optoelectronic properties of the respective QDs such as: (a)  $\eta_{LHE}$ ; (b) carrier separation and (c) carrier injection efficiency, as all the other components of the devices (photoanode, electrolyte and counter electrode) are the same. The optical measurements highlighted that the incorporation of alloyed  $(\text{CdSe}_x\text{S}_{1-x})_n$  ( $x = 0.5$ ,  $n = 4$ ) and graded alloyed  $(\text{CdSe}_x\text{S}_{1-x})_n$  ( $x = 0.1$ – $0.9$ ,  $n = 5$ ) interfacial layer significantly broadens the absorption spectra from 400 to 670 nm for CSA1 QDs and from 400 to 700 nm with small contribution up to 850 nm for CSA2 QDs with respect to CS QDs system from 400 to 620 nm [see Fig. 2(a)]. This confirmed the higher  $\eta_{LHE}$  for the devices using CSA2 QDs than the device with CSA1 QDs and CS QDs system, consistent with the observed trend of PV performance and EQE measurements of devices based on respective QDs.

Carrier dynamics measurements demonstrated that an exciton is photo-generated in QDs by the absorption of a photon. The exciton is then separated in electron and hole, mainly depending on the electronic band alignment between the core and shell of QDs. The shifts in PL peak positions of CSA1 QDs (648 nm) and CSA2 QDs (649 nm) with respect

to CS QDs (605 nm) is due to possible enhanced carrier delocalization in the shell region for CSA1 and CSA2 QDs respectively. The enhanced carrier delocalization is caused by the reduced interfacial confinement potential and defects at the sharp interface of CS QDs (as described above). In addition, carrier transport within the QDs is also a very promising factor to improve the PV performance of QDSCs. Calculated values of both  $K_{et}$  and  $K_{ht}$  from transient PL measurements follow the trend CSA2 QDs > CSA1 QDs > CS QDs as shown in Fig. 4. This trend is consistent with the observed PV performance of QDSCs based on the respective QDs as light harvesters.

In contrast, the theoretical calculations demonstrate the enhanced e-h spatial overlap area (%) for CSA2 and CSA1 QDs with respect to the CS QDs leads to higher e-h recombination probability and lower the overall  $\tau$  of the respective QDs. However, the lower value of  $\tau$  in CSA2 and CSA1 QDs compared to reference CS QDs seems less important due to the dominance of other appealing features of CSA2 and CSA1 QDs such as higher light harvesting efficiency in a broader range, better carrier separation and transport. Hence, this better PV performance of QDSCs based on CSA2 and CSA1 QDs than QDSCs based on CS QDs is caused by the excellent optoelectronic properties of the corresponding QDs.

In addition, to understand in greater detail the carrier dynamics of the QDSCs based CSA2, CSA1 and CS QDs, we applied transient photovoltage decay. This technique provides dynamic information on the carrier recombination processes which occurs at the  $\text{TiO}_2$ -MWCNTs/QDs/electrolyte interface. To measure transient photovoltage decay, all QDSCs were illuminated with a solar simulator under one sun simulated sunlight (AM 1.5G,  $100 \text{ mW/cm}^2$ ) until reaching a steady voltage, which is the  $V_{oc}$  of the QDSC. Then the simulator shutter was closed and the voltage decay with time was recorded for all QDSCs under dark conditions. Fig. 6(c) displays the  $V_{oc}$  decay curves versus time for all QDSCs based on CSA2, CSA1 and CS QDs system. The rate of  $V_{oc}$  decay

is slower in the case of QDSC with CSA2 QDs than the QDSCs with CSA1 and CS QDs. At particular time ( $s$ ) value, the  $V_{oc}$  decay rate follows the trend CSA2 QDs > CSA1 QDs > CS QDs [see Fig. 6(c)]. From the  $V_{oc}$  decay measurements, the electron life time ( $\tau_e$ ) was calculated by using the following equation [55,56].

$$\tau_e = -\left(\frac{k_B T}{e}\right)\left(\frac{dV_{oc}}{dt}\right)^{-1} \quad (3)$$

where  $k_B$  is Boltzmann's constant,  $T$  is the absolute temperature, and  $e$  is the electron's charge.

The  $\tau_e$  constant depends on the non-radiative carrier recombination at the TiO<sub>2</sub>-MWCNTs/QDs/electrolyte interface. As discussed above, the presence of alloyed and graded alloyed interfacial layers significantly improves the optoelectronic properties of CSA2 and CSA1 QDs with respect to CS QDs in terms of light harvesting efficiency, fast carrier separation and transport due to favorable stepwise band alignment (see Fig. 1). The calculated  $\tau_e$  value is higher for QDSCs based on CSA2 and CSA1 QDs as compared to QDSC based on CS QDs [see Fig. 6(d)]. At a particular  $V_{oc}$  ( $\sim 0.350$  V), the  $\tau_e$  of QDSCs based on the different shell structure and composition of QDs, follow the trend CSA2 QDs > CSA1 QDs > CS QDs as shown in Fig. 6(d). The higher value of  $\tau_e$  in the case of QDSCs with CSA2 QDs confirms the lower carrier recombination rate compared to QDSCs based on CSA1 and CS QDs. The suppressed non-radiative carrier recombination with the incorporation of alloyed and graded alloyed layers is due to the reduced interfacial confinement potential and defects created by the lattice mismatch (4.4%) between the CdSe core and CdS shell sharp interface of CS QDs [52]. This accelerates the carrier separation and injection process, as confirmed by transient PL decay and theoretical calculations. These results are consistent with the PV performances obtained for QDSCs based on the respective QDs systems.

#### 4. Conclusions and perspectives

In summary, we incorporated CdSe<sub>x</sub>S<sub>1-x</sub> interfacial layers between the CdSe core and CdS shell in heterostructured core/shell QDs. CSA1 QDs exhibit a broader absorption spectrum towards longer wavelength, better carrier separation, injection and transport rate compared to CS QDs, yielding a significantly enhanced PCE of 5.52%, which is 79% higher than the PEC of QDSCs based on CS QDs. To further improve the performance of QDSCs, the CdSe<sub>x</sub>S<sub>1-x</sub> interfacial layers were engineered by tailoring the Se:S molar ratios during in situ growth of each interfacial layer between CdSe core and CdS shell. The resulting new graded alloyed CSA2 QDs show a broader absorption response (400–700 nm), higher electron-hole transfer rate and modified confinement potential as compared to CSA1 and reference CS QDs. The QDSC based on CSA2 QDs exhibits the highest PCE of 7.14%, which is 29% higher than the QDSC based on CSA1 QDs. These results demonstrate that interfacial engineering can improve the optoelectronic properties of core/shell QDs, thus representing a promising approach to improve the performance of optoelectronic technologies based on QDs. Future directions will focus on the further improvement of the PV performance of QDSCs based on heterostructured core/shell QDs by optimizing the interfacial alloyed shell thickness/structure compositions and selection of different core and shell materials, such as PbS/CdPbS/CdS, CdTe/CdSeTe/CdSe, CuInS/CuInSSe/CuInSe “giant” QDs.

#### Acknowledgements

The authors acknowledge funding from the Natural Science and Engineering Research Council of Canada (NSERC), the Canada Foundation for Innovation (CFI) for infrastructure support and its operating funds. F.R. is grateful to the government of China for a Chang Jiang scholar short-term award and Sichuan province for a 1000 talent plan short-term award. F.R. acknowledges IFFS/UESTC for partial

funding of this work. F.R. is also grateful to the Canada Research Chairs program for funding and partial salary support. G.S.S. acknowledges the UNESCO Chair in MATECSS and the IFFS/UESTC for a PDF Excellence Scholarship. H. Zhang acknowledges the UNESCO Chair in MATECSS and FQRNT for PhD Excellence Scholarship. H. Zhao acknowledges start-up funds from Qingdao University and funding from the Natural Science Foundation of Shandong Province (ZR2018MB001).

#### Appendix A. Supplementary material

Supplementary data associated with this article can be found in the online version at doi:10.1016/j.nanoen.2018.11.001

#### References

- [1] S. Rühle, M. Shalom, A. Zaban, *Chem. Phys. Chem.* 11 (2010) 2290–2304.
- [2] (a) J. Tang, K.W. Kemp, S. Hoogland, K.S. Jeong, H. Liu, L. Levina, M. Furukawa, X. Wang, R. Debnath, D. Cha, K.W. Chou, A. Fischer, A. Amassian, J.B. Asbury, E.H. Sargent, *Nat. Mater.* 10 (2011) 765–771; (b) C. Piliego, L. Protesescu, S.Z. Bisri, M.V. Kovalenko, M.A. Loi, *Energy Environ. Sci.* 6 (2013) 3054–3059.
- [3] X. Wang, G.I. Koleilat, J. Tang, H. Liu, I.J. Kramer, R. Debnath, L. Brzozowski, D.A.R. Barkhouse, L. Levina, S. Hoogland, E.H. Sargent, *Nat. Photonics* 5 (2011) 480–484.
- [4] M.W. Knight, H. Sobhani, P. Nordlander, N.J. Halas, *Science* 332 (2011) 702–704.
- [5] M. Frasco, N. Chaniotakis, *Sensors* 9 (2009) 7266.
- [6] (a) X. Yang, K. Dev, J. Wang, E. Mutlugun, C. Dang, Y. Zhao, S. Liu, Y. Tang, S.T. Tan, X.W. Sun, H.V. Demir, *Adv. Funct. Mater.* 24 (2014) 5977–5984; (b) I. Moreels, Y. Justo, B. De Geyter, K. Hastraete, J.C. Martins, Z. Hens, *ACS Nano* 5 (2011) 2004–2012.
- [7] Y. Zhou, D. Benetti, Z. Fan, H. Zhao, D. Ma, A.O. Govorov, A. Vomiero, F. Rosei, *Adv. Energy Mater.* 6 (2016) 1501913.
- [8] (a) S. Chan, M. Liu, K. Latham, M. Haruta, H. Kurata, T. Teranishi, Y. Tachibana, *J. Mater. Chem. C* 5 (2017) 2182–2187; (b) I. Moreels, Y. Justo, B. De Geyter, K. Hastraete, J.C. Martins, Z. Hens, *ACS Nano* 5 (2011) 2004–2012.
- [9] W.W. Yu, L. Qu, W. Guo, X. Peng, *Chem. Mater.* 15 (2003) 2854–2860.
- [10] I.A. Ostapenko, G. Honig, C. Kindel, S. Rodt, A. Strittmatter, A. Hoffmann, D. Bimberg, *Appl. Phys. Lett.* 97 (2010) 063103.
- [11] O.E. Semonin, J.M. Luther, S. Choi, H.Y. Chen, J. Gao, A.J. Nozik, M.C. Beard, *Science* 334 (2011) 1530–1533.
- [12] W.A. Tisdale, K.J. Williams, B.A. Timp, D.J. Norris, E.S. Aydil, X.Y. Zhu, *Science* 328 (2010) 1543–1547.
- [13] P.V. Kamat, *J. Phys. Chem. Lett.* 4 (2013) 908–918.
- [14] V.I. Klimov, *J. Phys. Chem. B* 110 (2006) 16827–16845.
- [15] S. Jiao, J. Du, Z. Du, D. Long, W. Jiang, Z. Pan, Y. Li, X. Zhong, *J. Phys. Chem. Lett.* 8 (2017) 559–564.
- [16] E.M. Sanehira, A.R. Marshall, J.A. Christians, S.P. Harvey, P.N. Ciesielski, L.M. Wheeler, P. Schulz, L.Y. Lin, M.C. Beard, J.M. Luther, *Sci. Adv.* 3 (2017) 1–8.
- [17] H. Savin, P. Repo, G. Von Gastrow, P. Ortega, E. Calle, M. Garin, R. Alcubilla, *Nat. Nanotechnol.* 10 (2015) 624–628.
- [18] K.T. Cho, S. Paek, G. Grancini, C. Roldan-Carmona, P. Gao, Y. Lee, M.K. Nazeeruddin, *Energy Environ. Sci.* 10 (2017) 621–627.
- [19] J.-W. Lee, D.-Y. Son, T.K. Ahn, H.-W. Shin, I.Y. Kim, S.-J. Hwang, M.J. Ko, S. Sul, H. Han, N.-G. Park, *Sci. Rep.* 3 (2013) 1050.
- [20] F. Hetsch, X. Xu, H. Wang, S.V. Kershaw, A.L. Rogach, *J. Phys. Chem. Lett.* 2 (2012) 1879–1887.
- [21] I. Mora-Seró, S. Giménez, F. Fabregat-Santago, R. Gómez, Q. Shen, T. Toyoda, *J. Bisquert, Acc. Chem. Res.* 42 (2009) 1848–1857.
- [22] J. Wang, I. Mora-Seró, Z. Pan, K. Zhao, H. Zhang, Y. Feng, G. Yang, X. Zhong, *J. Bisquert, J. Am. Chem. Soc.* 135 (2013) 15913–15922.
- [23] S. Kim, B. Fisher, H.-J. Eisler, M. Bawendi, *J. Am. Chem. Soc.* 125 (2003) 11466–11467.
- [24] H. Zhu, N. Song, T. Lian, *J. Am. Chem. Soc.* 133 (2011) 8762–8771.
- [25] L. Etgar, D. Yanover, R.K. Čapek, R. Vaxenburg, Z. Xue, B. Liu, M.K. Nazeeruddin, E. Lifshitz, M. Grätzel, *Adv. Funct. Mater.* 23 (2013) 2736–2741.
- [26] Z. Ning, H. Tian, C. Yuan, Y. Fu, H. Qin, L. Sun, H. Agren, *Chem. Comm.* 47 (2011) 1536–1538.
- [27] B.N. Pal, Y. Ghosh, S. Brovelli, R. Laochareonsuk, V.I. Klimov, J.A. Hollingsworth, H. Htoon, *Nano Lett.* 12 (2012) 331–336.
- [28] B. Huang, R. Xu, N. Zhuo, L. Zhang, H. Wang, Y. Cui, J. Zhang, *Superlattice Microstruct.* 91 (2016) 201–207.
- [29] L. Jin, G. Sirigu, X. Tong, A. Camellini, A. Parisini, G. Nicotra, C. Spinella, H. Zhao, S. Sun, V. Morandi, M. Zavelani-Rossi, F. Rosei, A. Vomiero, *Nano Energy* 30 (2016) 531–541.
- [30] R. Adhikari, L. Jin, F. Navarro-Pardo, D. Benetti, B. Alotaibi, S. Vanka, H. Zhao, Z. Mi, A. Vomiero, F. Rosei, *Nano Energy* 27 (2016) 265–274.
- [31] G.S. Selopal, H. Zhao, X. Tong, D. Benetti, F. Navarro-Pardo, Y. Zhou, D. Barba, F. Vidal, Z.M. Wang, F. Rosei, *Adv. Funct. Mater.* 27 (2017) 1701468.
- [32] F. García-Santamaría, Y. Chen, J. Vela, R.D. Schaller, J.A. Hollingsworth,

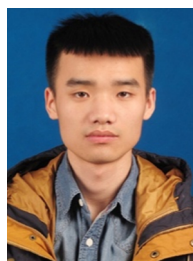
- V.I. Klimov, *Nano Lett.* 9 (2009) 3482–3488.
- [33] Y. Chen, J. Vela, H. Htoon, J.L. Casson, D.J. Werder, D.A. Bussian, V.I. Klimov, J.A. Hollingsworth, *J. Am. Chem. Soc.* 130 (2008) 5026–5027.
- [34] B. Lee, C.C. Stoumpos, N. Zhou, F. Hao, C. Malliakas, C.-Y. Yeh, T.J. Marks, M.G. Kanatzidis, R.P.H. Chang, *J. Am. Chem. Soc.* 136 (2014) 15379–15385.
- [35] B. Mahler, P. Spinicelli, S. Buil, X. Quelin, J.-P. Hermier, B. Dubertret, *Nat. Mater.* 7 (2008) 659–664.
- [36] F. Meinardi, A. Colombo, K.A. Velizhanin, R. Simonutti, M. Lorenzon, L. Beverina, R. Viswanatha, V.I. Klimov, S. Brovelli, *Nat. Photonics* 8 (2014) 392–399.
- [37] I. Coropceanu, M.G. Bawendi, *Nano Lett.* 14 (2014) 4097–4101.
- [38] A.M. Smith, A.M. Mohs, S. Nie, *Nat. Nanotechnol.* 4 (2009) 56–63.
- [39] V.E. Demidov, M.P. Kostylev, K. Rott, P. Krzyszczyk, G. Reiss, S.O. Demokritov, *Appl. Phys. Lett.* 95 (2009) 112509.
- [40] H. Zhao, D. Benetti, L. Jin, Y. Zhou, F. Rosei, A. Vomiero, *Small* 12 (2016) 5354–5365.
- [41] S. Jiao, J. Wang, Q. Shen, Y. Li, X. Zhong, *J. Mater. Chem. A* 4 (2016) 7214–7221.
- [42] W.K. Bae, Y.-S. Park, J. Lim, D. Lee, L.A. Padilha, H. McDaniel, I. Robel, C. Lee, J.M. Pietryga, V.I. Klimov, *Nat. Commun.* 4 (2013) 2661.
- [43] H. Zhao, G. Sirigu, A. Parisini, A. Camellini, G. Nicotra, F. Rosei, V. Morandi, M. Zavelani-Rossi, A. Vomiero, *Nanoscale* 8 (2016) 4217–4226.
- [44] B.O. Dabbousi, J. Rodriguez-Viejo, F.V. Mikulec, J.R. Heine, H. Mattoussi, R. Ober, K.F. Jensen, M.G. Bawendi, *J. Phys. Chem. B* 101 (1997) 9463–9475.
- [45] Y. Ghosh, B.D. Mangum, J.L. Casson, D.J. Williams, H. Htoon, J.A. Hollingsworth, *J. Am. Chem. Soc.* 134 (2012) 9634–9643.
- [46] K.T. Dembele, G.S. Selopal, C. Soldano, R. Nechache, J.C. Rimada, I. Concina, G. Sberveglieri, F. Rosei, A. Vomiero, *J. Phys. Chem. C* 117 (2013) 14510–14517.
- [47] Q. Shen, K. Katayama, T. Sawada, M. Yamaguchi, T. Toyoda, *Jpn. J. Appl. Phys.* 45 (2006) 5569–5574.
- [48] S. Brovelli, R.D. Schaller, S.A. Crooker, F. Garcia-Santamaria, Y. Chen, R. Viswanatha, J.A. Hollingsworth, H. Htoon, V.I. Klimov, *Nat. Commun.* 2 (2011) 280.
- [49] H. McDaniel, N. Fuke, N.S. Makarov, J.M. Pietryga, V.I. Klimov, *Nat. Commun.* 4 (2013) 2887.
- [50] W.K. Bae, L.A. Padilha, Y.S. Park, H. McDaniel, I. Robel, J.M. Pietryga, V.I. Klimov, *ACS Nano* 7 (2013) 3411–3419.
- [51] H. Zhu, N. Song, W. Rodriguez-Cordoba, T. Lian, *J. Am. Chem. Soc.* 134 (2012) 4250–4257.
- [52] S.A. Ivanov, A. Piryatinski, J. Nanda, S. Tretiak, K.R. Zavadil, W.O. Wallace, D. Werder, V.I. Klimov, *J. Am. Chem. Soc.* 129 (2007) 11708–11719.
- [53] B. Blackman, D.M. Battaglia, T.D. Mishima, M.B. Johnson, X. Peng, *Chem. Mater.* 19 (2007) 3815–3821.
- [54] S.S. Shin, J.S. Kim, J.H. Suk, K.D. Lee, D.W. Kim, J.H. Park, I.S. Cho, K.S. Hong, J.Y. Kim, *ACS Nano* 7 (2013) 1027–1035.
- [55] J. Bisquert, F. Fabregat-Santiago, I. Mora-Sero, G. Garcia-Belmonte, S. Gimenez, *J. Phys. Chem. C* 113 (2009) 17278–17290.
- [56] A. Zaban, M. Greenshtein, J. Bisquert, *ChemPhysChem.* 4 (2003) 859–864.



**Guiju Liu** received her Bachelor degree in Materials Physics from Qingdao University (China) in 2014. She obtained Master degree at Qingdao University (China) in 2017. Currently, she is a Ph.D. student majoring in Materials Physics and Chemistry at Qingdao University. Her research mainly focuses on the synthesis and structural characterization of quantum dots and their applications in luminescent solar concentrators and hydrogen generation.



**Hui Zhang** received his Bachelor's degree in Materials Physics and Master's degree in Materials Engineering from Sichuan University, China, in June 2012 and June 2015, respectively. During his Master study, his research focused on nanocomposite materials and their applications in electrochemistry. He is currently a Ph.D. student under the joint supervision of Prof. Federico Rosei and Prof. Shuhui Sun at INRS-EMT supported by UNESCO Chair in MATECSS and FRQNT for Ph.D. Excellence Scholarships, conducting research on design and synthesis of quantum dots for solar technologies.



**Xin Tong** obtained his bachelor's degree from School of Microelectronics and Solid-State Electronics, University of Electronic Science and Technology of China (UESTC) in 2014. He is currently a joint Ph.D. student in Institute of Fundamental and Frontier Sciences, UESTC and Institut National de la Recherche Scientifique (INRS, Canada). His research interests focus on the design and synthesis of colloidal quantum dots and their applications in solar technologies.



**Kanghong Wang** received his Bachelor Degree in Material Science and Engineering from Northeastern University, China. He obtained Master Degree at the Institute of Functional Nano & Soft Materials (FUNSOM), Soochow University. He is currently working as a Ph.D. student at Institut National de la Recherche Scientifique (INRS, Canada), conducting research on quantum dot solar cells and QDs based photoelectrochemical electrode for H<sub>2</sub> generation.



**Jie Tang** is a chief researcher and group leader of the Advanced Low Dimensional Nano Materials Group at the National Institute of Materials Science, Japan, a professor at Tsukuba University, Japan, an adjunct professor at The University of North Carolina at Chapel Hill, and a professor of Qingdao University, China. She received her B.S. degree in material science from Tsinghua University, China, and Ph.D. degree in physics from Osaka University, Japan. Her research interests include high pressure physics, electron emission materials, and graphene supercapacitors for energy storage applications.



**Gurpreet Singh Selopal** received his Ph.D. degree in Material for Engineering at CNR-INO SENSOR LAB of the University of Brescia, Italy in 2014. He is currently a post-doctoral fellow under the joint project of Institute of Fundamental and Frontier Sciences, University of Electronic Science and Technology of China and UNESCO chair at the Institut National de la Recherche Scientifique (INRS, Canada). His research work is mainly focused on the design and synthesis of nanostructured semiconductor materials and their applications in solar technologies such as third generation excitonic solar cells and solar-driven water splitting.



**Haiguang Zhao** is Professor of College of Physics & State Key Laboratory, Qingdao University, Qingdao (Shandong), China. He received M.Sc. degree (2007) from Zhejiang University and Ph.D. degree (2012) from Institut National de la Recherche Scientifique (INRS), Quebec University. His research interests focus on the synthesis of low-dimensional semiconductor materials (including metal oxide, quantum dot, nanoplatelets and inorganic perovskite) for solar energy applications, such as solar cell, luminescent solar concentrator and solar-driven water splitting.



**Xuhui Sun** is a full professor at the Institute of Functional Nano & Soft Materials (FUNSOM) at Soochow University. He received his Ph.D. degree from the City University of Hong Kong in 2002. He performed postdoctoral research at the University of Western Ontario, Canada from 2003 to 2005 and at NASA Ames Research Center, USA from 2005 to 2007. He became a research scientist at NASA and adjunct assistant professor at Santa Clara University in 2007. His research interests include nanoelectronics, energy harvesting, nanosensors, and the development and application of synchrotron radiation techniques.



**Yiqian Wang** received his Ph.D. degree in condensed matter physics from Institute of Physics, Chinese Academy of Sciences, China in 2001. Then he worked as a research fellow at INRS-EMT, Canada and Imperial College London, UK. He is currently a Professor at Qingdao University. His research interest includes the fabrication and characterization of perovskite functional materials, as well as exploitation of their potential applications.



**Shuhui Sun** directs the Laboratory of Sustainable Nanotechnology (SUN) at the Institut National de la Recherche Scientifique (INRS), center for Energy, Materials, and Telecommunications, Canada. Prof. Sun's current research interests focus on multifunctional nanomaterials for Energy and Environment, including PEM fuel cells (low-Pt and Pt-free catalysts), Li-/Na-/Zn-ion batteries, metal-air batteries, as well as water treatment. His several recent awards include the member of Global Young Academy, ECS-Toyota Young Investigator Fellow, IUPAC Novel Materials Youth Prize, and Canada Governor General's Academic Gold Medal.



**Zhiming M. Wang** received his B.S. degree in applied physics from Qingdao University, Qingdao, China, in 1992, his M.S. degree in physics from Peking University in Beijing, China, in 1995, and his Ph.D. degree in condensed matter physics from the Institute of Semiconductors at the Chinese Academy of Sciences in Beijing, China, in 1998. He is currently a Professor of National 1000-Talent Program, working in the University of Electronic Science and Technology of China. His research interests include the optoelectronic properties of low-dimensional semiconductor nanostructures and corresponding applications in photovoltaic devices.



**François Vidal** works on the theory and numerical modeling of various physical phenomena. After obtaining a Ph.D. from the University of Montreal (Canada) in Subatomic Physics, he worked as a research associate at CEA (France) and at INRS in the field of plasma physics. He then became a professor at INRS in 2003. In the last few years, he has been interested in materials science, in particular on DFT modeling of multiferroic materials and catalysis phenomena.



**Federico Rosei** is Professor and Director of the INRS Center Énergie, Matériaux et Télécommunications, Varennes (QC) Canada. He holds the UNESCO Chair in Materials and Technologies for Energy Conversion, Saving and Storage and the Senior Canada Research Chair in Nanostructured Materials. He received M.Sc. and Ph.D. degrees from the University of Rome "La Sapienza" in 1996 and 2001, respectively. He has received several awards and is Fellow/Member of many prestigious societies and academies, including the Royal Society of Canada, the European Academy of Sciences, the American Physical Society, the World Academy of Arts and Science, the Chinese Chemical Society (Honorary), the American Association for the

Advancement of Science, SPIE, the Canadian Academy of Engineering, ASM International and the Engineering Institute of Canada.